

## Seismic response of buried reservoir structures: a comparison of numerical simulations with centrifuge experiments

E. Esmailzadeh Seylabi<sup>a</sup>, C. Jeong<sup>b</sup>, S. Dashti<sup>c</sup>, A. Hushmand<sup>c</sup>, E. Taciroglu<sup>d,\*</sup>

<sup>a</sup> Mechanical & Civil Engineering Department, California Institute of Technology, Pasadena, CA 91125, USA

<sup>b</sup> Department of Civil Engineering, The Catholic University of America, Washington, DC 20064, USA

<sup>c</sup> Civil, Environmental & Architectural Engineering Department, University of Colorado Boulder, Boulder, CO 80309, USA

<sup>d</sup> Civil & Environmental Engineering Department, University of California, Los Angeles, CA 90095, USA

### ARTICLE INFO

#### Keywords:

Soil-structure interaction  
Underground reservoir structures  
Centrifuge testing  
Equivalent linear soil  
Domain reduction method  
Perfectly matched layer  
Principal component analysis

### ABSTRACT

Centrifuge experiments on seismic performance of relatively stiff underground reservoir structures in dry sand are modeled numerically. The capabilities of numerical simulations with calibrated equivalent linear soil properties in capturing the main features of experimentally measured responses are explored for both low and high amplitude earthquake motions. The scattering effects of the centrifuge container boundaries are also investigated by modeling the same soil deposit resting on an elastic bedrock and extending infinitely laterally, using the domain reduction method. It is observed that the calibrated equivalent linear soil models perform well in predicting accelerations, racking, and bending strains on the buried structure, even for high amplitude motions for which significant soil nonlinearity is expected. While not as accurate, the seismic lateral earth pressures predicted with these models are in fair agreement with direct measurements made with tactile sensors. The mismatches in earth pressures are likely due to local nonlinearities of soil and frictional contact, which were absent from the numerical models. It is also observed that the scattering effects of the container boundaries become more significant closer to the soil surface, and their characteristics are seen to depend on both the side boundaries and the embedded structure's stiffness.

### 1. Introduction

Seismic response of underground structures is a complex soil-structure interaction problem influenced by (i) the structure's geometry, inertia, and stiffness, (ii) the soil heterogeneity and nonlinearity, and (iii) the input motion characteristics. Existing methods for analyzing the responses of such structures are usually based on simplified analytical or numerical methodologies and their ranges of applicability are not yet adequately validated against physical model studies (see, for example, [1]).

Recently, Hushmand et al. [2] conducted a series of centrifuge experiments at the University of Colorado Boulder to investigate the seismic performance of relatively stiff structures buried in dry sand. Three different simplified box structures were designed to represent the characteristics of prototype reinforced concrete reservoir structures with varying stiffnesses. These structures were restrained from excessive rotational movements at the top and the bottom by their roofs and floors. Investigation of these experimental results showed that commonly used procedures could not adequately capture the loadings and deformations experienced by this class of underground structures

for the ranges of stiffness and the sets of ground motions regularly considered in their design [2]. This is mainly because these procedures are usually based either on the assumption of a yielding (e.g., [3]) or a rigid-unchanging wall (e.g., [4]). A yielding wall is expected to deform enough to result in an active or yielding condition in the backfill soil, while a rigid-unchanging wall undergoes no deformation. The structures of interest in this study are expected to deform, depending on their flexural stiffness, but their deformation is restrained. Therefore, these structures do not fall in either of the commonly assumed categories.

Although soil behavior can be highly nonlinear during strong shaking, use of nonlinear soil constitutive models may not always be practical due to general complexities in calibrating their numerous parameters (e.g., [5]). In the present study, we explore the capabilities of calibrated equivalent linear soil models in capturing the seismic response of buried box structures as observed in centrifuge tests. Dynamic soil properties are determined by calibrating the model parameters such that numerically predicted accelerations of the far-field soil column in the centrifuge test match the measurements. We also examine the effects of boundary conditions prescribed in the numerical models on the predicted response of buried structures. For this purpose, we use the so-

\* Corresponding author.

E-mail address: [etacir@ucla.edu](mailto:etacir@ucla.edu) (E. Taciroglu).

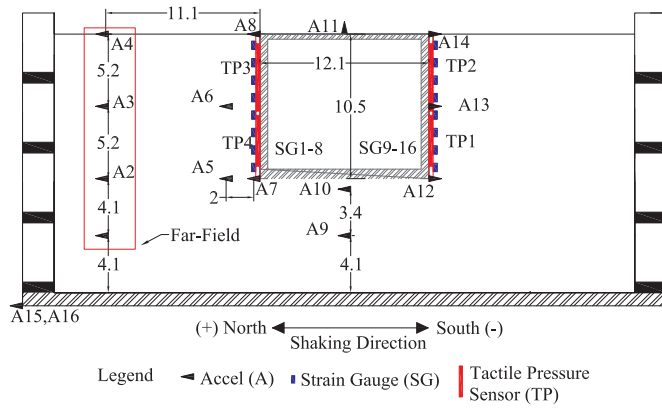


Fig. 1. Layout of the centrifuge tests studied (dimensions in prototype scale meters)[2].

called domain reduction method (DRM) [6,7] to model the same problem in a heterogeneous soil deposit on an elastic bedrock. We also use perfectly matched layers (PMLs) [8,9] as absorbing boundaries to truncate the semi-infinite extent of soil, which is particularly important when extending the numerical simulations beyond the inherently peculiar boundary conditions of centrifuge tests.

### 2. An overview of the centrifuge tests

The centrifuge test layout and instrumentation are shown in Fig. 1. Dimensions and properties of the model structures used for the experiments are provided in Table 1. The density, Young’s modulus and Poisson’s ratio of the steel specimen structures were 7870 kg/m<sup>3</sup>, 200 GPa, and 0.29, respectively. Dry Nevada sand with the specific gravity of  $G_s = 2.65$ , minimum and maximum void ratios of, respectively,  $e_{min} = 0.56$ ,  $e_{max} = 0.84$ , median diameter of  $D_{50} = 0.13$  mm, and uniformity coefficient of  $C_u = 1.67$  was pluviated inside a flexible shear beam container such that an approximately uniform soil layer with a dry unit weight of 15.6 kN/m<sup>3</sup> or a relative density ( $D_r$ ) of approximately 60% could be achieved.

Fig. 2 shows the 5%-damped spectral accelerations and the Arias Intensity time-histories of the base motions recorded in the centrifuge. Here, numerical results are presented and compared with experimental recordings for four cases that cover a range of stiffness and ground motion intensities. These are, specifically, “flexible” and “stiff” buried structures that were subjected to “Northridge-L” and “Northridge-H” motions (henceforth referred to as AL and AH). The experiments on the flexible and stiff structures will be referred to as T-Flexible and T-Stiff, respectively. The properties of the Northridge-L and H motions as recorded during the T-Flexible-AL and AH experiments are tabulated in Table 2. The mean frequency is the reciprocal of the mean period [10], and the predominant frequency is the frequency at which the maximum 5%-damped spectral acceleration occurs.

### 3. Numerical modeling of the centrifuge experiments

In the numerical simulations, only the soil inside the container and the structure are modeled. 8-noded quadratic elements are used for the discretization of both the soil and the structure. The finite element (FE)

Table 1  
Dimensions and properties of model structures in prototype scale.

Structure	Thickness			Fundamental frequency (Hz)
	Base (m)	Roof (m)	Walls (m)	
Flexible	0.5	0.28	0.28	1.9
Baseline	0.69	0.37	0.56	3.9
Stiff	1.46	1.12	1.13	9.1

code developed by Esmailzadeh et al. (see, [9], for details) is used to solve the plane strain elastodynamic heterogeneous half-space problems at hand. The element size is chosen such that approximately 12 discretized nodes exist within the minimum wavelength [11]. It is assumed that the interface of the structure and soil is perfectly bonded. Since a flexible shear beam container is used for the experiments—which can mimic free-field conditions for vertically propagating shear waves at its two side boundaries—, periodic boundary conditions are imposed on the horizontal degrees of freedom at the left and right vertical edges of the domain, while their vertical degrees of freedom are fixed. This numerical model is referred to as NM1 in subsequent analyses. Both the structure and the soil are assumed to exhibit linear elastic responses. The properties of the structure are the same as those provided in the previous section. The equivalent linear soil properties are obtained through an optimization-based procedure. Details of this procedure are provided next.

#### 3.1. Optimization of equivalent linear properties for the soil domain

The accelerations recorded by sensors A1, A2, A3, and A4 (cf. Fig. 1) are used to optimize the shear wave velocity profile as well as the equivalent viscous damping of the soil domain. It is assumed that the soil density is constant and is equal to 15.6 kN/m<sup>3</sup>. The relationship proposed by Rovithis et al. [12] is used to define the general form of a shear wave velocity profile, as in

$$V_s = V_H \left[ b + (1 - b) \frac{z}{H} \right]^n \tag{1}$$

where  $b = (V_0/V_H)^{1/n}$ ;  $n$  is the dimensionless inhomogeneity factor;  $z$  is the downward vertical coordinate measured from the soil surface; and  $V_0$  and  $V_H$  are shear wave velocities at  $z = 0$  and  $z = H$ , respectively. Soil damping is approximated using the Rayleigh damping model, as in

$$\begin{bmatrix} \xi_1 \\ \xi_2 \end{bmatrix} = \begin{bmatrix} 1/4\pi f_1 & \pi f_1 \\ 1/4\pi f_2 & \pi f_2 \end{bmatrix} \begin{bmatrix} a_0 \\ a_1 \end{bmatrix} \tag{2}$$

where  $f_1$  and  $f_2$  are the control frequencies;  $\xi_1$  and  $\xi_2$  are the associated damping ratios; and  $a_0$  and  $a_1$  are the coefficients to define the viscous damping matrix as a function of mass and stiffness matrices, respectively. Although usually the first- and third-mode frequencies of the soil columns are used for determination of control frequencies in site response analyses, it has been reported that selection of controlling frequencies can influence the response of the system significantly and that this choice should be made such that the system does not experience significant over damping in the dominant range of frequencies [13,14]. As a result, in this study, all four parameters ( $f_1, f_2, \xi_1, \xi_2$ ) are considered as the optimization parameters.

For any given set of shear wave velocity parameters ( $V_0, V_H, n$ ) and Rayleigh damping parameters ( $f_1, f_2, \xi_1, \xi_2$ ), we solve a one dimensional (1D) wave propagation problem of a soil column subjected to seismic input motion at its rigid base. The acceleration responses at locations A1, A2, A3, and A4 in the far-field soil column are then computed to define the following minimization problem:

$$\min_{\mathbf{x}} f(\mathbf{x}) = \frac{1}{2} \sum_{i=1}^{i=4} \sum_{j=1}^{j=n} E_i^*(\omega_j) E_i(\omega_j) \tag{3}$$

where  $E_i(\omega_j) = \sqrt{|A_i^e(\omega_j)|} [A_i^e(\omega_j) - A_i(\omega_j)]$ ;  $(\cdot)^*$  denotes the conjugate transpose of its subtended variable;  $A_i^e(\omega_j)$  and  $A_i(\omega_j)$  are the complex-valued experimental and numerical acceleration responses of the  $i$ th sensor at radial frequency  $\omega_j$ , respectively, in frequency domain; and  $\mathbf{x} = (V_0, V_H, n, \xi_1, \xi_2, f_1, f_2)$  is the optimization variable vector. Only the frequency range of 0–10 Hz is considered for this optimization problem.

In total, we solve the aforementioned optimization problem for four separate cases. The resulting optimal parameters are provided in Table 3. The variation of the shear wave velocity profile with depth as well as the variation of the Rayleigh damping model with frequency are

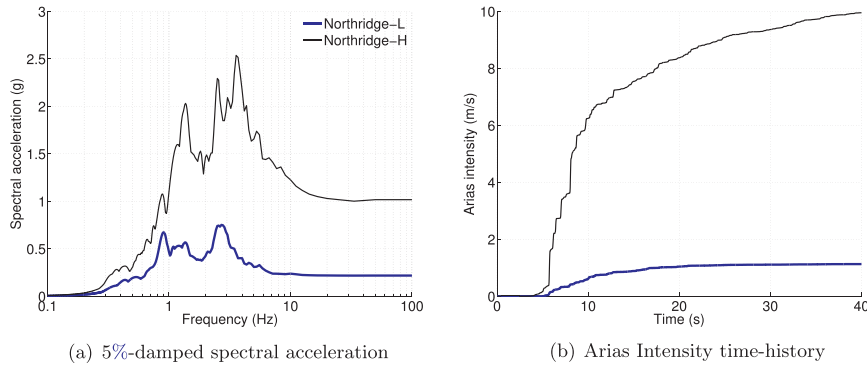


Fig. 2. (a) 5%-damped spectral accelerations and (b) Arias Intensity time-histories of the container base motions recorded for the test on flexible structure.

Table 2  
Properties of the base motions as recorded in T-Flexible.

Base motion	PGA	Arias Intensity	Significant	Mean frequency	Predominant
Name	(g)	$I_A$ (m/s)	Duration $D_{5-95}$ (s)	$f_m$ (Hz)	Frequency $f_p$ (Hz)
Northridge-L	0.22	1.13	16.18	1.19	2.70
Northridge-H	1.02	9.95	25.91	1.44	3.57

Table 3  
Optimized shear wave velocity profile and Rayleigh damping model coefficients.

Test	$V_0$ (m/s)	$V_H$ (m/s)	$n$	$f_1$ (Hz)	$f_2$ (Hz)	$\xi_1$	$\xi_2$
T-Flexible-AL	23.5	142.0	1.00	1.00	3.36	0.34	1
T-Stiff-AL	22.2	147.0	0.81	0.84	2.32	0.31	0.66
T-Flexible-AH	22.3	114.7	0.90	1.25	3.33	0.45	1
T-Stiff-AH	15.4	124.3	0.72	1.25	3.50	0.44	1

shown in Fig. 3. In general, one may use the free-field soil column to obtain the dynamic soil properties as prescribed above, and we note here that the results using the far-field soil column in Fig. 1 were consistent with those of a free-field centrifuge experiment without any structures present.

Fig. 4 shows the 5%-damped spectral accelerations for the far-field array in each test along with those obtained from the 1D wave propagation analyses using the optimized dynamic soil properties. The Rayleigh damping curve is also shown. For low amplitude motions—i.e., T-Flexible-AL and T-Stiff-AL—there is good agreement between the 1D simulation results and those obtained from the far-field array

experimentally. The agreement slightly deteriorates for the strong motion cases—i.e., T-Flexible-AH and T-Stiff-AH—, and this may be attributed to the higher level of soil nonlinearity, scattering effects, and spurious resonances that may happen in an equivalent linear soil model.

It is known that the first natural frequency of the uniform soil layer on rigid bedrock is  $V_s/4H$  where  $V_s$  is the shear wave velocity and  $H$  is the height of the soil layer. Here, in order to obtain the natural frequencies of the nonuniform soil layer with properties shown in Table 3, we compute the stiffness matrix  $\mathbf{K}$  and mass matrix  $\mathbf{M}$  of the soil column. Then, with the assumption of classical damping, we compute the eigenvalues of the matrix  $\mathbf{M}^{-1}\mathbf{K}$ . Table 4 shows the resulting natural frequencies for the considered cases.

In order to have a closer look at the contribution of soil's damped natural frequencies as well as the predominant and mean frequencies of the base motion (see Table 2), we compute the time-frequency distributions (TFDs) of the energy densities for acceleration time-series at locations A15 (base), A4 (far-field surface), and A14 (structure surface). Fig. 5 shows the resulting TFDs for each signal in T-Flexible-AL and AH. For T-Flexible-AL, the first damped natural frequency of the far-field soil column is very close to the mean frequency of the base motion. As shown, for both A14 and A15, the signal energy also increases around the predominant frequency of the base motion. This is while the signal energy at A4 is more influenced by the soil dynamic properties. The correlation between the first damped natural frequency of the soil layer and the mean frequency of the base motion decreases in T-Flexible-AH. This may be attributed to the fact that the measured accelerations at the base of the centrifuge container are always influenced by the dynamic properties of the container, soil, and the structure. For lower amplitude motions, these effects may become more significant.

In both cases, however, we expect the system response to be more dominated by the soil deposit free vibration as we approach the end of

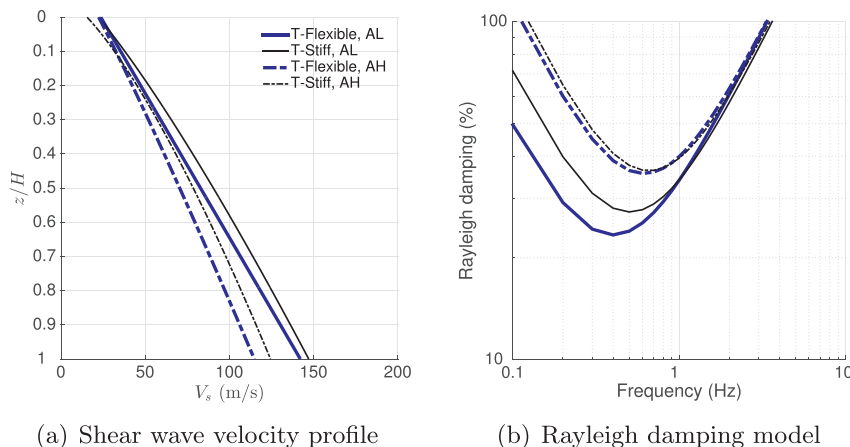


Fig. 3. The optimized (a) shear wave velocity profile and (b) Rayleigh damping model.

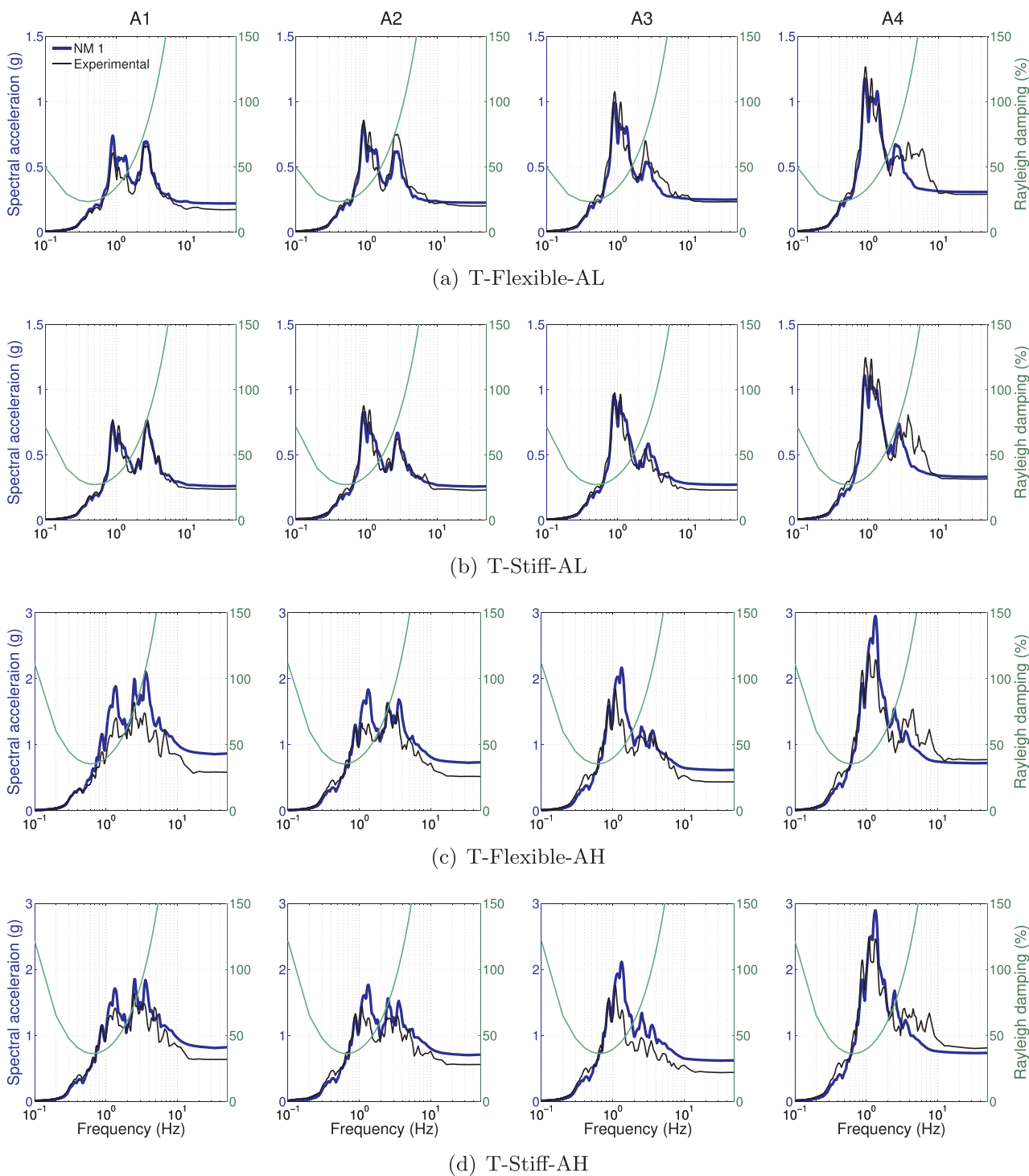


Fig. 4. 5%-spectral acceleration obtained from far-field array in the experiment and from the 1D wave propagation analysis using optimized dynamic soil properties.

**Table 4**  
The first three natural frequencies of the soil column with the optimized dynamic properties.

Test	$f_1$ (Hz)	$f_2$ (Hz)	$f_3$ (Hz)
T-Flexible-AL	1.23	2.81	4.52
T-Stiff-AL	1.33	3.01	4.84
T-Flexible-AH	1.05	2.44	3.95
T-Stiff-AH	1.15	2.56	4.08

the signal's duration. This can already be seen in T-Flexible-AH in Fig. 5 as the signal energy is concentrated around a frequency of 1 Hz. In T-Flexible-AL, we compute the TFD of the modulated signals such that the signal amplitude remains constant with time. Fig. 6 shows the TFD of the modulated signals for T-Flexible-AL. As shown, the signal energy becomes more significant around the fundamental frequency of the far-field soil column after  $t = 25$  s, which is also in agreement with the significant duration of the base motion. Moreover, traces of soil non-linearity can be seen in these figures—namely, frequency increases, which are likely due to soil densification, and temporary frequency decreases, which are likely due to soil hysteresis.

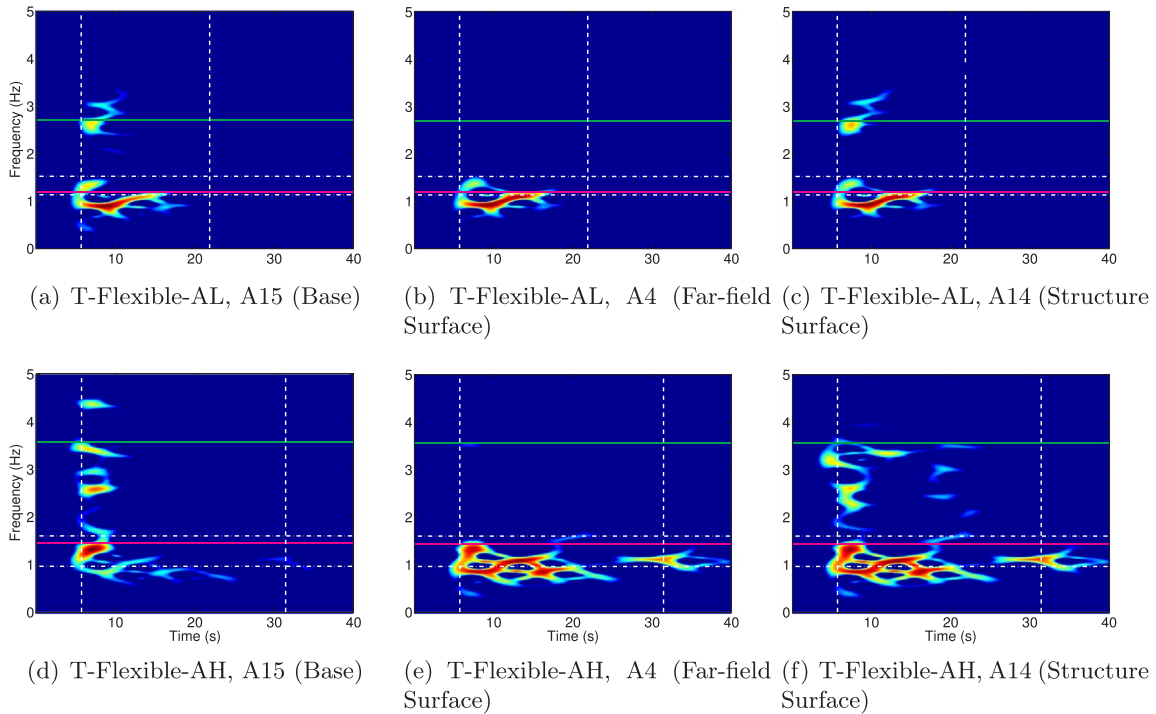


Fig. 5. TFDS of acceleration time-series for T-Flexible-AL and AH; horizontal white dashed lines are the first two damped natural frequencies of the far-field soil column; horizontal green solid line is the predominant frequency of the base motion; magenta horizontal solid line is the mean frequency of the base motion; vertical white dashed lines span the significant duration of the base motion.

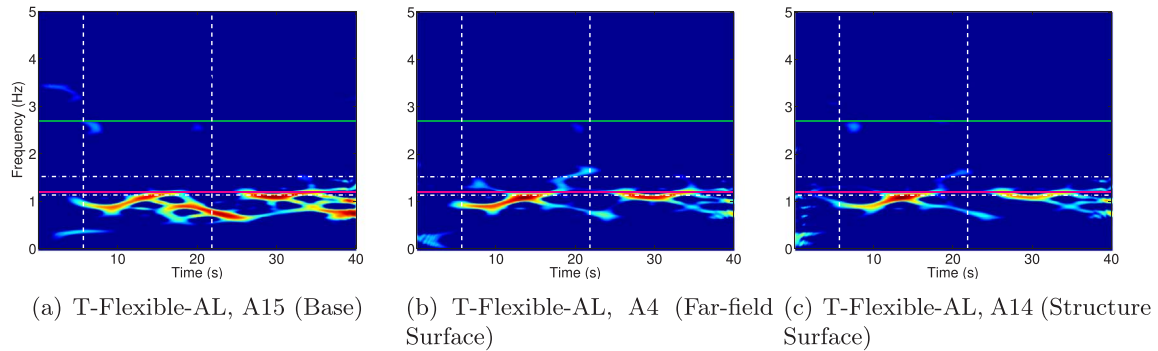


Fig. 6. TFDS of modulated acceleration time-series for T-Flexible-AL; horizontal white dashed lines are the first two damped natural frequencies of the far-field soil column; horizontal green solid line is the predominant frequency of the base motion; magenta horizontal solid line is the mean frequency of the base motion; vertical white dashed lines span the significant duration of the base motion.

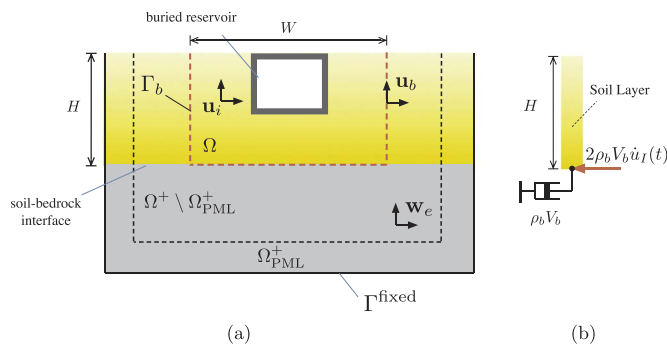


Fig. 7. Schematic configuration of (a) the PML truncated soil-structure model subjected to effective input force vectors in the framework of DRM and (b) an auxiliary problem of a 1D wave propagation within a soil domain on elastic bedrock.

### 3.2. Quantification of scattering due to centrifuge container boundaries

In order to quantify the spurious effects of the rigid base and the periodic boundaries—which mimic a flexible shear beam container—on the response of numerically modeled buried structures, we use the domain reduction method (DRM) to model the same soil deposit with depth  $H = 18.6$  m and width  $W = 42$  m that rests on an elastic bedrock and extends to infinity laterally. DRM is a two-step finite element procedure proposed by Bielak et al. [7] for modeling the seismic responses of highly heterogeneous subdomains. The primary advantage of this method is that the size of the computational domain can be reduced significantly by introducing appropriate absorbing boundaries if one is only interested in the response of a localized feature—e.g., the response of a structure and its surrounding soil deposit.

The configuration of the problem, which is referred to as NM2 in subsequent analyses, is shown schematically in Fig. 7a. As shown,  $\mathbf{u}_i$  and  $\mathbf{u}_b$  are total wave response fields inside the soil deposit  $\Omega$  and along the DRM interface  $\Gamma_b$ , respectively, and  $\mathbf{w}_e$  is the scattered wave response field within  $\Omega^+$ . Since the waves outside the fictitious boundary

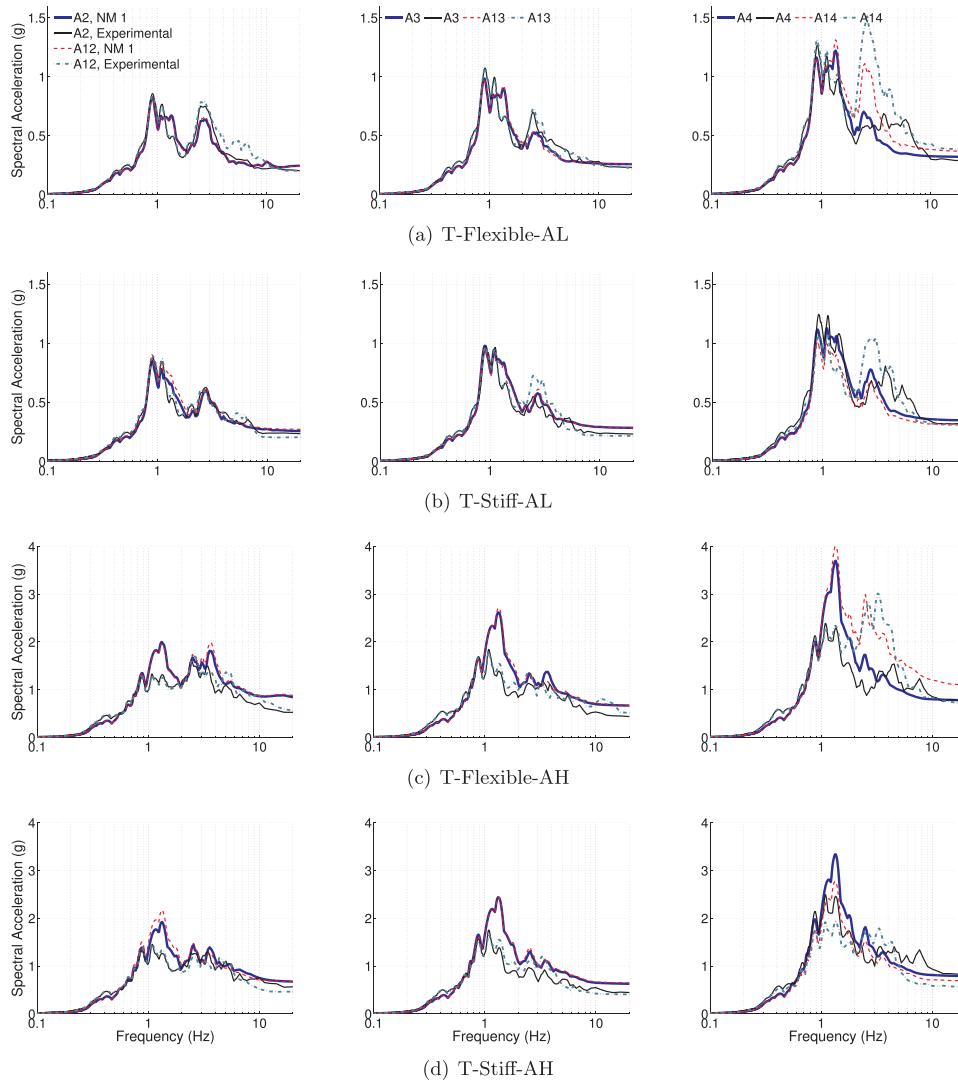


Fig. 8. 5% damped spectral acceleration at far-field (A2, A3, A4) and on structure (A12, A13, A14) for T-Flexible-AL, Stiff-AL, Flexible-AH, and Stiff-AH obtained numerically and experimentally.

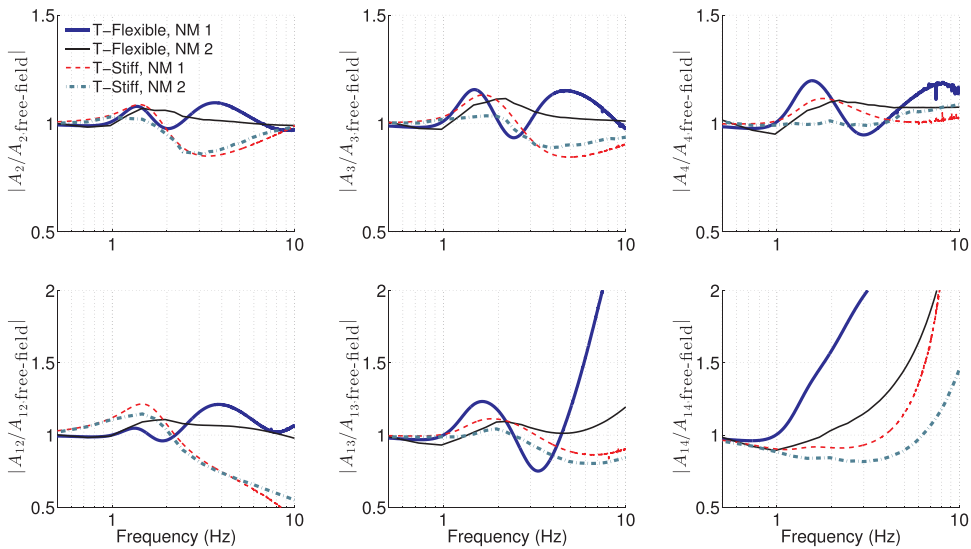


Fig. 9. Amplitude of scattering transfer functions for NM1 (numerical model with rigid base and periodic side boundaries) and NM2 (numerical model with elastic bedrock and laterally infinite soil extent) for T-Flexible-AL and T-Stiff-AL.

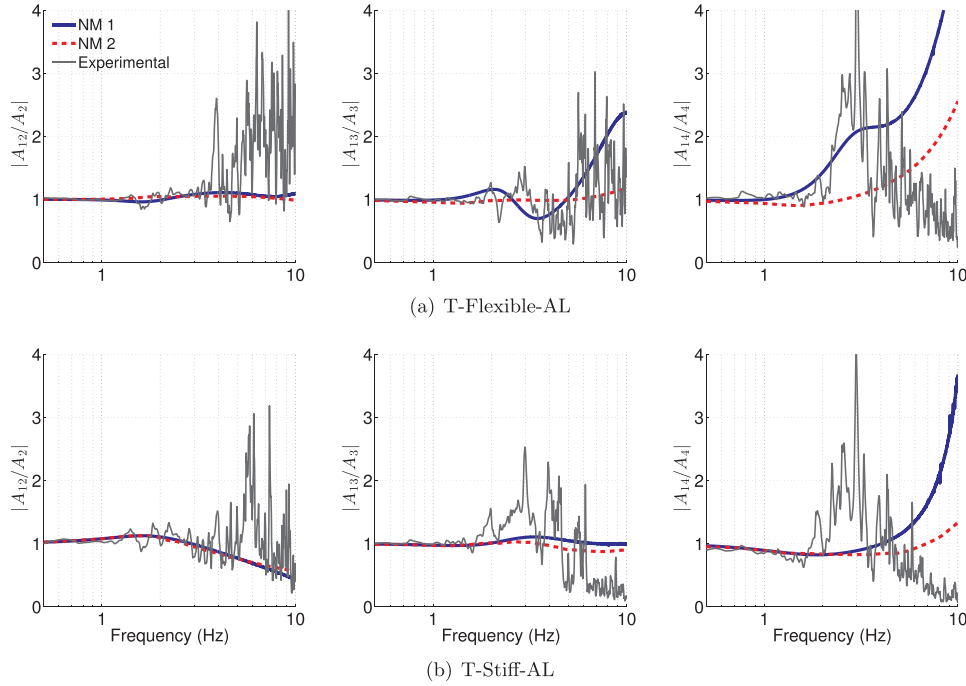


Fig. 10. Numerical and experimental amplitude of the structure to far-field soil transfer functions for T-Flexible-AL and T-Stiff-AL.

$\Gamma_b$  are all outgoing, we use perfectly matched layers (PML) for absorbing the scattered field in  $\Omega^+$  and therefore making the size of the model finite while avoiding any spurious reflections from the fixed boundary  $\Gamma^{\text{fixed}}$  [8,9] that may occur when using other types of absorbing boundaries such as the Lysmer-Kuhlemeyer dashpots.

In order to solve the scattering problem shown in Fig. 7a, we need to compute the effective input force vector  $\mathbf{p}^{\text{eff}}$ . Partitioning the wave field as  $[\mathbf{u}_i^T \ \mathbf{u}_b^T \ \mathbf{w}_e^T]^T$ ,  $\mathbf{p}^{\text{eff}}$  can be defined as follows [6,7]:

$$\mathbf{p}^{\text{eff}} = \begin{bmatrix} \mathbf{p}_b^{\text{eff}} \\ \mathbf{p}_b^{\text{eff}} \\ \mathbf{p}_e^{\text{eff}} \end{bmatrix} = \begin{bmatrix} \mathbf{0} \\ -\bar{\mathbf{M}}_{bb}^{\Omega^+} \ddot{\mathbf{u}}_b^0 + \bar{\mathbf{C}}_{bb}^{\Omega^+} \dot{\mathbf{u}}_b^0 + \bar{\mathbf{K}}_{bb}^{\Omega^+} \mathbf{u}_b^0 \\ \bar{\mathbf{M}}_{eb}^{\Omega^+} \ddot{\mathbf{u}}_b^0 + \bar{\mathbf{C}}_{eb}^{\Omega^+} \dot{\mathbf{u}}_b^0 + \bar{\mathbf{K}}_{eb}^{\Omega^+} \mathbf{u}_b^0 \end{bmatrix} \quad (4)$$

where  $\mathbf{u}_b^0$  and  $\mathbf{p}_b^0$  are the free-field displacements and forces along the fictitious boundary  $\Gamma_b$ . Matrices  $\bar{\mathbf{A}}_{bb}^{\Omega^+}$  and  $\bar{\mathbf{A}}_{eb}^{\Omega^+}$  with  $(\mathbf{A} = \mathbf{M}, \mathbf{C} \text{ or } \mathbf{K})$  are obtained using the following partitioning:

$$\bar{\mathbf{A}}^{\Omega^+} = \begin{bmatrix} \bar{\mathbf{A}}_{bb}^{\Omega^+} & \bar{\mathbf{A}}_{be}^{\Omega^+} \\ \bar{\mathbf{A}}_{eb}^{\Omega^+} & \bar{\mathbf{A}}_{ee}^{\Omega^+} \end{bmatrix}. \quad (5)$$

The free-field response can be obtained from solving an auxiliary problem in which the localized feature (the buried reservoir in this study) is removed [7]. Here, we are interested in the response of the buried structure and the soil deposit under vertically propagating shear waves. Therefore, the free-field information can be computed efficiently by (i) solving a 1D wave propagation problem of a heterogeneous viscoelastic soil layer of height  $H$  on an elastic bedrock, and by subsequently (ii) mapping the resulting displacements and forces along  $\Gamma_b$ .

As shown in Fig. 7b, in a 1D free-field analysis, we replace the homogeneous elastic undamped bedrock by a dashpot with coefficient  $\rho_b V_b$ . The terms  $\rho_b$  and  $V_b$  refer to the density and shear wave velocity of the elastic bedrock, respectively. The incoming waves are applied to the truncated model by prescribing a force equal to  $2\rho_b V_b \dot{u}_i(t)$  at a degree of freedom where the dashpot is attached [15]. The term  $\dot{u}_i(t)$  refers to the particle velocity of incoming SV waves at  $z = H$  in the free-field

condition.

In the centrifuge test,  $\ddot{u}_g(t)$ —i.e., the base motion of the container—is known and is prescribed at the rigid bedrock in the NM1 numerical simulations. This motion is usually referred to as the *within motion*. Here, we assume that this motion is the same as the *outcrop motion*. Therefore, we assume that  $u_g(t) = 2u_i(t)$ . Further details on the implementation of DRM in a PML-truncated heterogeneous half-space and its verification can be found in [16,17].

#### 4. Comparison of numerical and experimental results

In this section, we explore the capability of the numerical simulations in capturing the main features of the conducted centrifuge experiments in terms of acceleration, racking, bending strains, and dynamic lateral earth pressures along the walls of the structures in tests T-Flexible-AL, T-Stiff-AL, T-Flexible-AH, and T-Stiff-AH.

##### 4.1. Accelerations

Fig. 8 compares the 5%-damped spectral accelerations obtained numerically and experimentally at different locations for different tests. During the low amplitude base motion, in which we expect less soil nonlinearity, the numerically computed spectral accelerations are in good agreement with their experimental counterparts at all locations. Discrepancies at higher frequencies are mainly due to overdamping of the numerical model which becomes significant at location A14 (i.e., on top of the buried structure). During high amplitude motions, as we get closer to the soil surface, discrepancies between the equivalent-linear soil model and experimental accelerations increase both in the far-field and on the structure. These discrepancies are correlated with frequency amplitude spectra shown in Fig. 4.

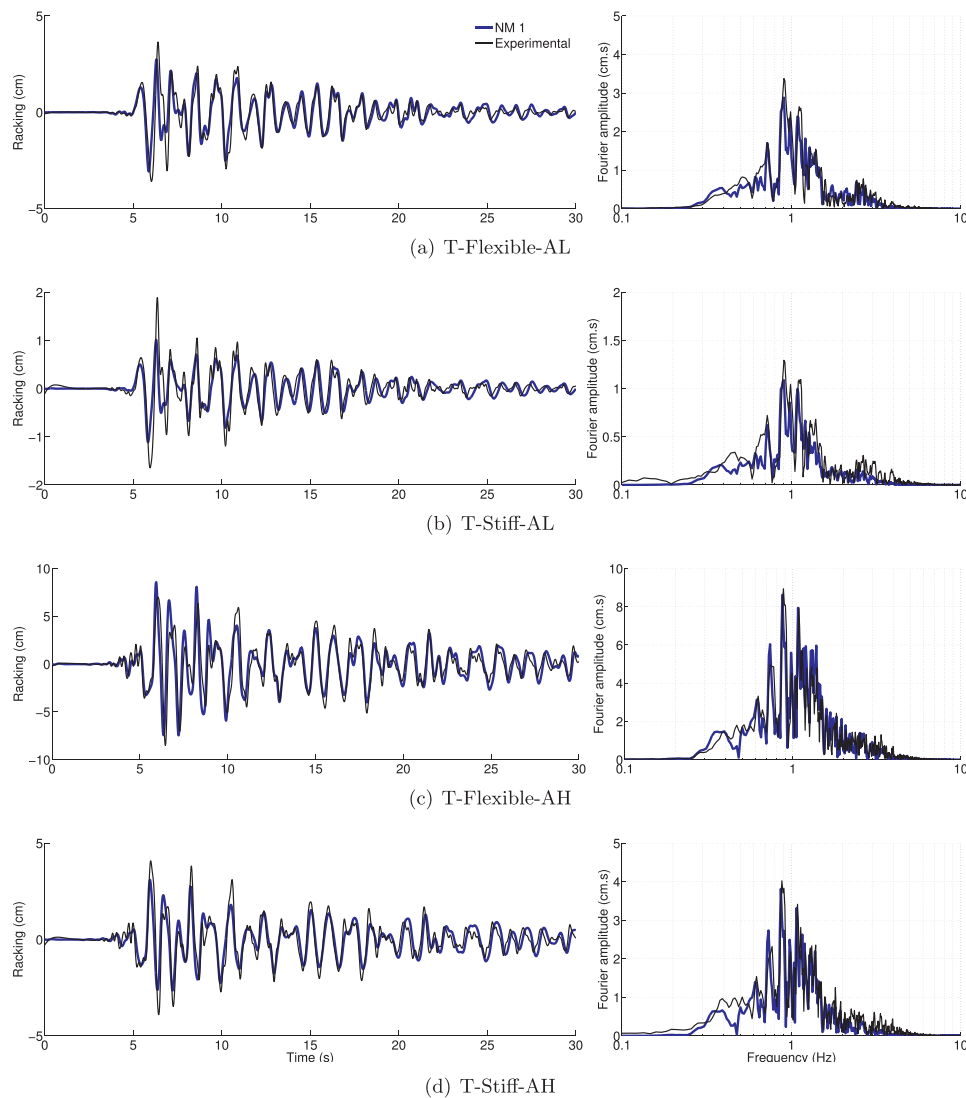


Fig. 11. Time-series and Fourier amplitude of the experimental and numerical racking of the south wall of the structures.

In order to explore the effects of the assumed boundary conditions on the responses of the far-field soil and structure, we use the NM2 numerical modeling approach described in the previous section to compute the response of the same soil deposit and structure resting on an elastic bedrock. It is assumed that  $\rho_b = 15.6 \text{ kN/m}^3$  and  $V_b = 450 \text{ m/s} \approx 3V_H$ .

The scattering effects in both numerical models—i.e., NM1 and NM2—are quantified by computing the scattering transfer function  $A_i/A_{i,\text{free-field}}$ .  $A_i$  is the Fourier transform of the acceleration response at location  $i$  (see Fig. 1) and  $A_{i,\text{free-field}}$  is the Fourier transform of the corresponding free-field acceleration response. The latter is computed by numerical modeling of the studied cases with no structure (i.e., soil-only).

Fig. 9 shows the amplitude of the computed transfer functions. As described above, NM1 is the numerical model with the assumption of a rigid bedrock and periodic side boundaries; NM2 is the numerical model with the elastic bedrock and laterally semi-infinite soil. The main observations are as follows:

- As the frequency increases, the scattering effects become more significant. This is mainly because at small frequencies all particles move in-phase with each other and therefore the scattering effects diminish. This is in agreement with trends of kinematic transfer functions observed for embedded foundations and retaining walls

e.g., [17].

- The far-field response is influenced by scattering, even for NM2, due to its proximity to the buried structure. Depending on the stiffness of the structure and the input excitation frequency, it may result in amplification or de-amplification of the scattering transfer functions. Existence of a rigid bedrock as well as the periodic boundaries in NM1 can accentuate the effects of constructive and destructive interferences, especially for T-Flexible-AL.
- The scattering amplification in T-Stiff-AL is generally smaller than those in T-Flexible-AL, which is in agreement with experimental observations on tested structures [5], and may be partly due to the higher inertial forces from the flexible structure.

In order to compare the numerical and experimental results, we also compute the ratios of the structural and far-field acceleration responses. Fig. 10 displays the amplitude of the resulting transfer functions. For experimental data, we use the procedure suggested by Mikami et al. [18] to reduce the noise levels in the computed transfer functions. A 0.2 Hz Hamming window with 21 points is used for smoothing the power spectral densities of the acceleration time-series. Despite discrepancies at higher frequencies, the experimental transfer functions are in good agreement with those obtained from the numerical models.

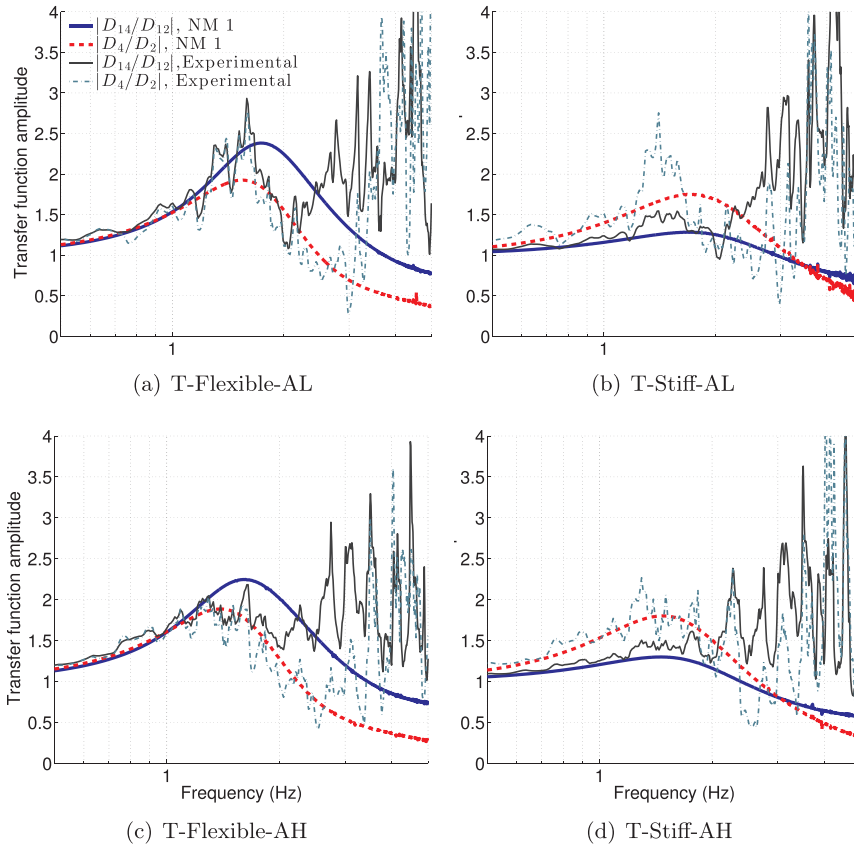


Fig. 12. The total displacement transfer functions obtained from numerically computed displacements and experimentally measured accelerations in the far-field and on the structure.

### 4.2. Racking of the structure

Racking deformation is generally defined as the relative lateral displacement of the roof of the buried structure with respect to its base, and is an important parameter in displacement-based design procedures for buried structures. In order to compute the racking deformation from the experimental data, we double-integrate the accelerations at locations A14 and A12, and subtract the latter from the former. For the numerical models, racking can be computed directly by subtracting the total displacements at A12 from A14. As shown in Fig. 11, the numerical and experimental results are in a good agreement for all cases.

Fig. 12 shows the transfer functions of total displacements for the structure and the far-field between surface and at depth, which can be used to evaluate scattering effects in different models. For numerically computed transfer functions, the peak of the transfer function for the flexible structure is larger than that of the far-field transfer function. This is reversed for the stiff structure. Moreover, as the frequency increases, the far-field transfer functions obtained for T-Flexible and T-Stiff start deviating from each other, which illuminates the difference in scattering effects for the flexible and stiff structures on the far-field soil. Further, it is seen that the numerical transfer functions better trace the experimental ones for the stiff structure.

### 4.3. Bending strains

Bending strains and moments are an important measure of the seismic performance of buried structures and are used regularly in design. In order to measure the bending strain along the walls of the structures in centrifuge, 8 strain gauges were installed outside of each wall. In numerical simulations, for reservoir elements with one side in contact with soil, we compute the tangential strain at the center of the element side. Fig. 13 shows the numerically computed and experimentally measured strain values at the location of SG8 shown in Fig. 1,

at the bottom of the north wall. For both structures (flexible and stiff) the numerical and experimental results are in a good agreement. It should be mentioned that a low-pass Butterworth filter is used to reduce the noise in strain data measured for the stiff structure.

In order to have a closer look at the spatial distribution and temporal variation of bending strains along the structure wall, we use the method of principal component analysis. We first create the data matrix:  $\mathbf{X} = [\mathbf{e}_1 \ \mathbf{e}_2 \ \dots \ \mathbf{e}_n]^T$  where  $\mathbf{e}_j$  for  $j = 1, 2, \dots, n$  is a strain time-series at location  $i$ . We then compute the correlation matrix:  $\mathbf{R} = \mathbf{X}\mathbf{X}^T/N$ , where  $N$  is the total number of data points of the time-series. We next obtain the Eigen decomposition of the matrix  $\mathbf{R}$ , which is  $\mathbf{R} = \mathbf{\Phi}\mathbf{\Lambda}^2\mathbf{\Phi}^T$ .  $\mathbf{\Phi} = [\mathbf{\Phi}_1 \dots \mathbf{\Phi}_n]$  contains the so-called mode shape vectors  $\mathbf{\Phi}_i$  and  $\mathbf{\Lambda}$  is a diagonal matrix with entries  $\lambda_i$  to be the  $i$ -th singular value of the matrix  $\mathbf{X}$ . We finally compute the so-called modal contribution coefficients, which are given through the matrix  $\mathbf{Q} = [\mathbf{q}_1 \dots \mathbf{q}_n]^T = \mathbf{\Phi}^T\mathbf{X}$ .

Fig. 14 shows the first and second principal components of the numerical results and those obtained from experimental data. As seen, for all cases numerical simulations can capture both spatial and temporal variations of the experimentally measured bending strains successfully. The discrepancies in the second mode of the stiff structure are due to the noise level in experimental data. In general, we expect the contribution of the second mode to be less for the stiff structure. Participation of the principal components shown in Fig. 14 can be quantified through the Eigenvalues of the correlation matrix, using

$$E_{\lambda_i} = \frac{\lambda_i^2}{\sum_{i=1}^n \lambda_i^2} \quad \text{for } i = 1, \dots, n. \tag{6}$$

The resulting values for the first and second modes are provided in Table 5, which shows the significant contribution of the first mode in all cases.

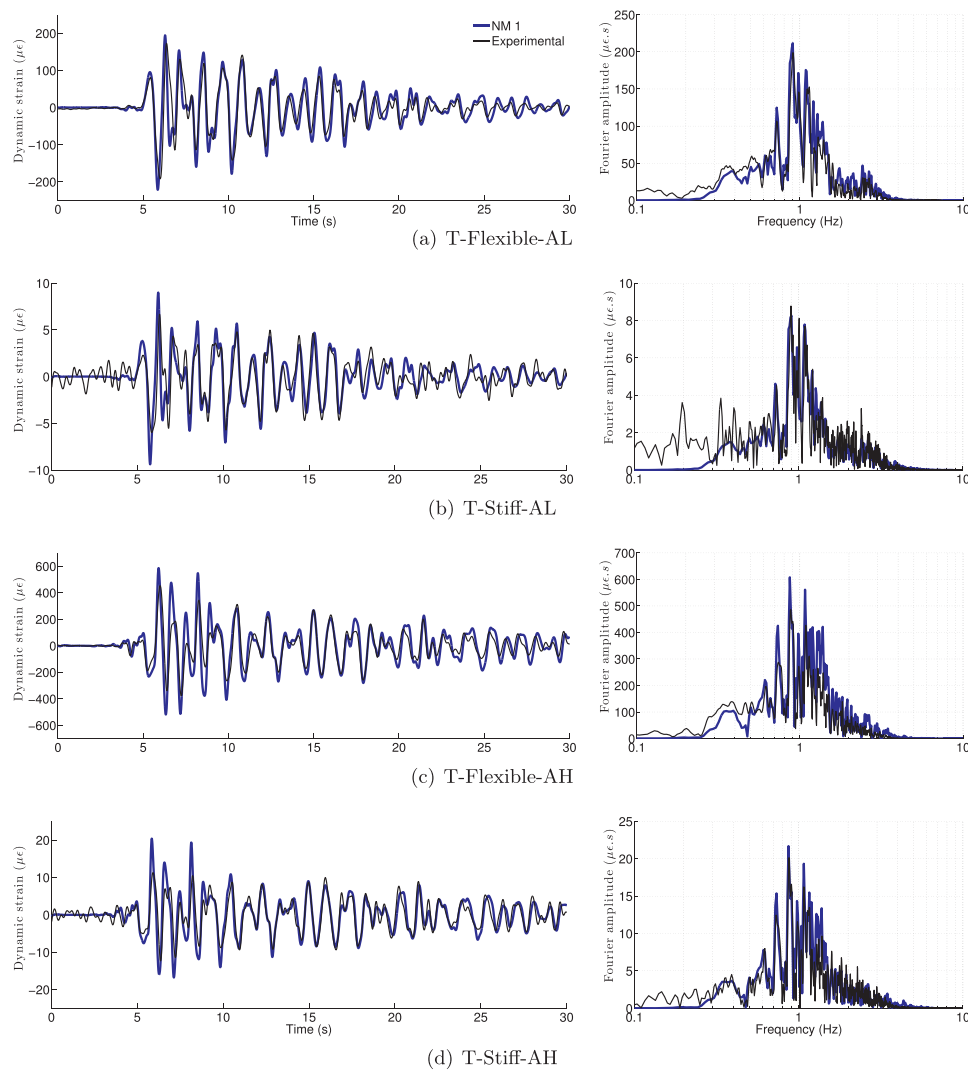


Fig. 13. Time-series and Fourier amplitude of the experimentally measured and numerically computed dynamic bending strain of the sensor SG8 at the bottom of the north wall.

#### 4.4. Dynamic lateral earth pressures on the structure walls

Dynamic lateral earth pressures were experimentally measured on the walls of buried structures using tactile pressure sensors (manufactured by Tekscan Inc.) that were statically and dynamically calibrated as detailed by Gillis et al. [19]. Data was averaged over each row of sensing elements to reduce scatter [2]. The authors have given significant effort to understand and calibrate the tactile sensors for this particular application; nevertheless, earth pressures in dynamic centrifuge experiments are difficult to measure reliably. Therefore, there is an inherently higher degree of uncertainty in earth pressure measurements than, for example, strain measurements. As such, the quality of agreement between the directly measured and predicted earth pressures may not be as high as other quantities of interest.

To compute dynamic earth pressures numerically, first the normal nodal forces applied on the walls are computed at their interface with soil elements. Then, normal stresses are obtained at the center of the edge of each element by dividing the nodal force by the length of the element edge. We use the same procedure described in the previous section to obtain the spatial and temporal variations of the dynamic stresses along the walls of specimen structures. Fig. 15 shows the resulting distributions for both experimental and numerical data. As shown, for the flexible structure, even though the temporal variations of the first principal component are slightly underestimated, the spatial distributions are captured well. For the stiff structure, on the other

hand, capturing the spatial distribution is not as successful as that of the more flexible structure. This may be attributed partially to the perfect-bond assumption used for the soil-structure interface modeling in numerical analyses, to local soil nonlinearities, as well as, to some extent, the uncertainties in experimental recordings (particularly since dynamic strains compared very well).

## 5. Conclusions

In this study, we used the finite element method for numerical simulations of a series of centrifuge experiments conducted on buried reservoir structures in dry sand. Due to complexities of nonlinear soil models, we examined the capabilities of the equivalent linear soil model in capturing experimentally measured responses. We used an optimization based method to calibrate the shear wave velocity profile and the Rayleigh damping model of a soil column using the available far-field acceleration data. We observed that the numerical simulations with the calibrated equivalent linear dynamic soil properties could capture the measured accelerations, racking, bending strains and dynamic earth pressures with acceptable accuracy even for the high amplitude base motion. Therefore, for the soil and structural properties evaluated in this study and in the absence of experimental results, one can use the results of nonlinear site response analyses of a soil column to calibrate the equivalent linear soil model properties. Then two-dimensional linear wave propagation analyses can be conducted for the

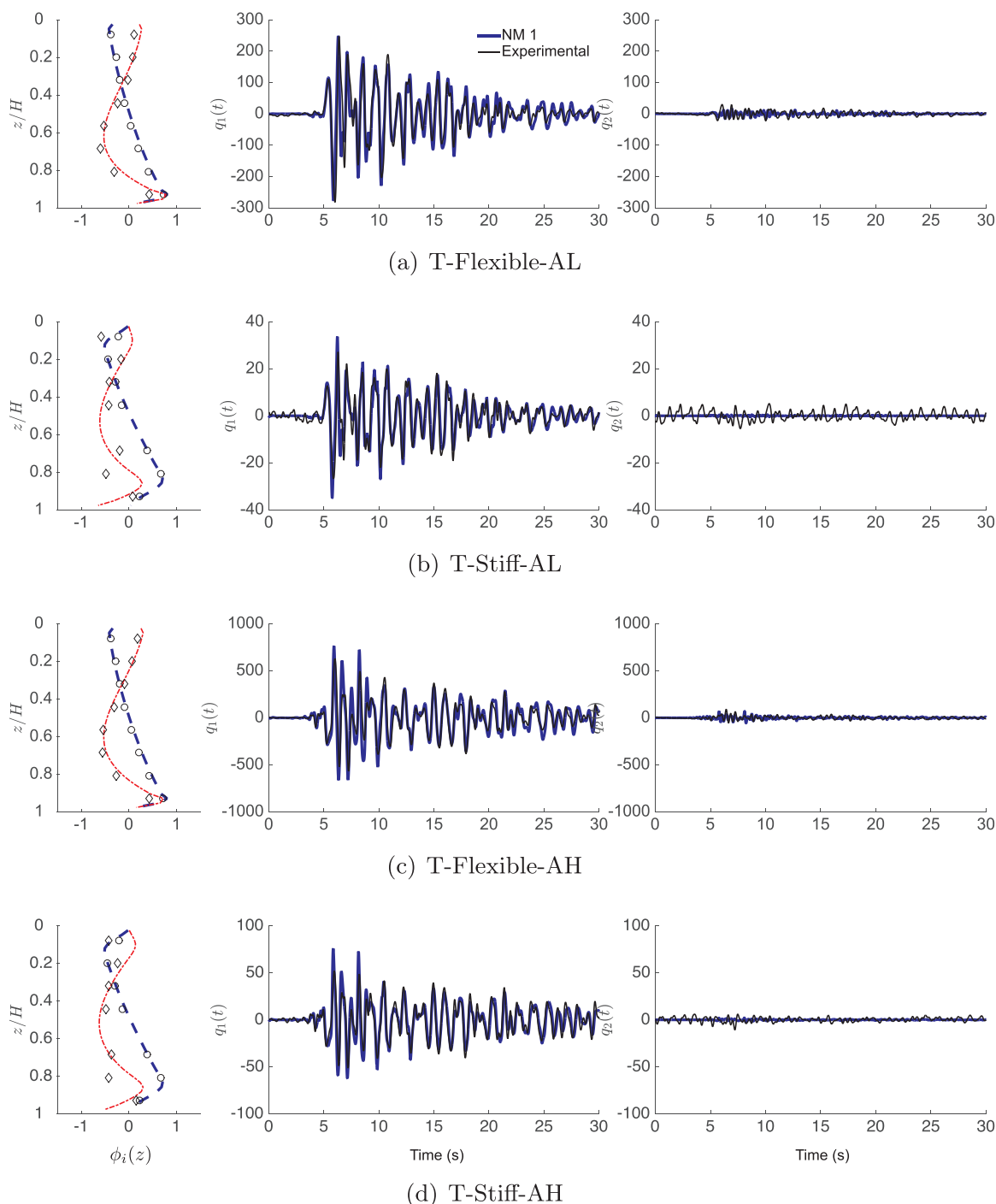


Fig. 14. Spatial distribution and temporal variation of the first two principal components of the dynamic bending strain along the walls of the structures; for subplots on the left, NM1 ( $i = 1$ ) - - - - -, NM1 ( $i = 2$ ) - - - - -, Experimental ( $i = 1$ )  $\circ$ , Experimental ( $i = 2$ )  $\diamond$ .

Table 5  
Energies of the first and second principal components of numerical and experimental strain data.

Test	NM1		Experimental	
	$E_{\lambda_1}(\%)$	$E_{\lambda_2}(\%)$	$E_{\lambda_1}(\%)$	$E_{\lambda_2}(\%)$
T-Flexible-AL	99.54	0.34	97.98	1.30
T-Stiff-AL	99.97	0.03	84.07	7.75
T-Flexible-AH	99.58	0.33	98.70	1.00
T-Stiff-AH	99.94	0.05	95.25	2.37

numerical simulation of a buried structure. On the other hand, models featuring contact procedures at the soil-structure interface as well as nonlinear soil models may be necessary to more accurately capture seismic earth pressures [20].

Due to the limited width and height of the centrifuge containers, it is not possible to study the behavior of deep soil deposits with large lateral extents resting on elastic bedrock by directly using centrifuge measurements. The numerical modeling methodology described herein, on the other hand, enables the exploration of realistic site conditions when designing underground reservoir structures for seismic loading. In the said approach, we used the domain reduction method to inject the far-field seismic input motion into a computational domain truncated

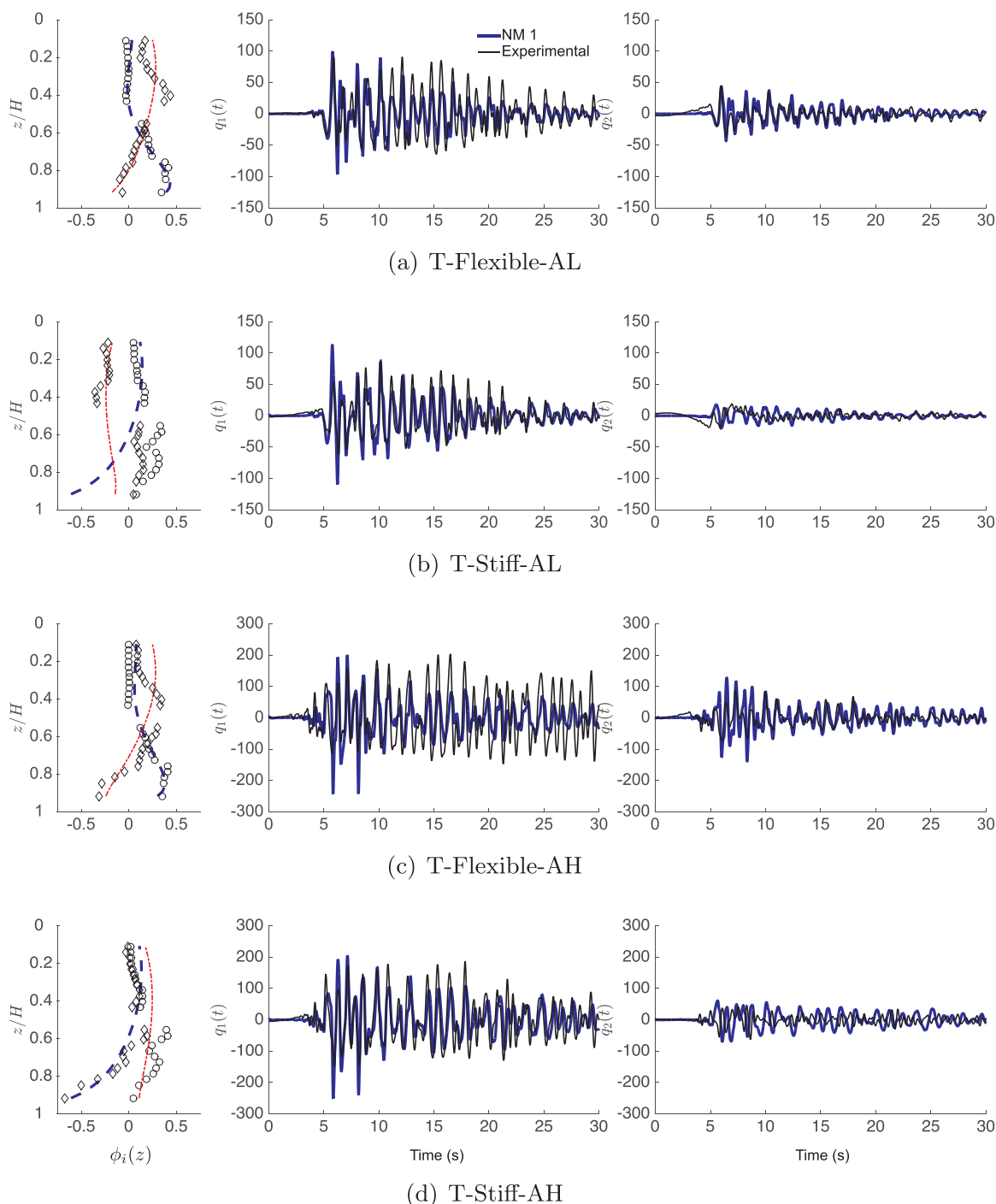


Fig. 15. Spatial distribution and temporal variation of the first two principal components of the dynamic stresses along the walls of the structures; for subplots on the left, NM1 ( $i = 1$ ) — — —, NM1 ( $i = 2$ ) - · - · -, Experimental ( $i = 1$ ) ○, Experimental ( $i = 2$ ) ◇.

by perfectly matched layers. The transfer functions computed from such models showed that the centrifuge container boundaries significantly affect the measured responses, especially near soil surface. Moreover, the scattering effects of the centrifuge container are coupled with the specimen stiffness. Therefore, the primary utility of the centrifuge tests are to calibrate and validate numerical models, with which the design parameter space of buried structures can be explored, rather than providing findings that can be directly generalized.

**Acknowledgements**

The authors would like to acknowledge the support from the Los

Angeles Department of Water and Power (LADWP) for the centrifuge experiments presented in this study, and the guidance and support provided by Dr. Craig Davis and Dr. Ben Hushmand in designing and conducting the centrifuge tests.

**References**

[1] Pitilakis K, Tsiniadis G. *Earthquake Geotechnical Engineering Design*. Vol. 28 of *Geotechnical, Geological and Earthquake Engineering*. Springer; 2014. p. 279–340. Ch. 11.  
 [2] Hushmand A, Dashti S, Davis C, Hushmand B, Zhang M, Ghayoomi M, McCartney JS, Lee Y, Hu J. Seismic performance of underground reservoir structures: insight from centrifuge modeling on the influence of structure stiffness. *J Geotech*

- Geoenviron Eng 2016;142(7):04016020.
- [3] Seed HB, Whitman RV. Design of earth retaining structures for dynamic loads. in: ASCE Specialty Conference, Lateral Stresses in the Ground and Design of Earth Retaining Structures, 1970, p. 103–147.
- [4] Wood JH. Earthquake induced soil pressures on structures. Ph.D. Thesis, California Institute of Technology (1973).
- [5] Deng YH, Dashti S, Hushmand A, Davis C, Hushmand B. Seismic response of underground reservoir structures in sand: evaluation of class-c and c1 numerical simulations using centrifuge experiments. *Soil Dyn Earthq Eng* 2016;85:202–16.
- [6] Bielak J, Christiano P. On the effective seismic input for non-linear soil-structure interaction systems. *Earthq Eng Struct Dyn* 1984;12:107–19.
- [7] Bielak J, Loukakis K, Hisada Y, Yoshimura C. Domain reduction method for three dimensional earthquake modeling in localized regions, part i: theory. *Bull Seismol Soc Am* 2003;93:817–24.
- [8] Kucukcoban S, Kallivokas L. A symmetric hybrid formulation for transient wave simulations in pml-truncated heterogeneous media. *Wave Motion* 2013;50(1):57–79.
- [9] Esmailzadeh Seylabi E, Jeong C, Taciroglu E. On numerical computation of impedance functions for rigid soil-structure interfaces embedded in heterogeneous half-spaces. *Comput Geotech* 2016;72:15–27.
- [10] Rathje EM, Abrahamson NA, Bray JD. Simplified frequency content estimates of earthquake ground motions. *J Geotech Geoenviron Eng* 1998;124(FEBRUARY):150–9.
- [11] Bao H, Bielak J, Ghattas O, Kallivokas LF, O'Hallaron DR, Shewchuk JR, et al. Large-scale simulation of elastic wave propagation in heterogeneous media on parallel computers. *Comput Methods Appl Mech Eng* 1998;152(1):85–102.
- [12] Rovithis EN, Parashakis H, Mylonakis GE. 1d harmonic response of layered inhomogeneous soil: analytical investigation. *Soil Dyn Earthq Eng* 2011;31:879–90.
- [13] Park D, Hashash Y. Soil damping formulation in nonlinear time domain site response analysis. *J Earthq Eng* 2004;8:249–74.
- [14] Hashash Y, Groholski DR, Phillips C. Recent advances in nonlinear site response analysis. In: *Proceedings of the 5th International Conference on Recent Advances in Geotechnical Earthquake Engineering*, 2010.
- [15] Zhang Y, Yang Z, Bielak J, Conte JP, Elgamal A. Treatment of seismic input and boundary conditions in nonlinear seismic analysis of bridge ground system. In: *Proceedings of the 16th ASCE Engineering Mechanics Conference*, University of Washington, Seattle, 2003.
- [16] Seylabi EE. Reduced order modeling of soil structure interaction problems. Ph.D. Thesis, University of California, Los Angeles (2016).
- [17] Esmailzadeh Seylabi E, Zhang W, Jeong C, Taciroglu E. On dynamic responses of underground box structures. In: *Proceedings of the 3rd International Conference on Performance-based Design in Earthquake Geotechnical Engineering (PBD-III)* (paper no. 398), 2017.
- [18] Mikami A, Stewart JP, Kamiyama M. Effects of time series analysis protocols on transfer functions calculated from earthquake accelerograms. *Soil Dyn Earthq Eng* 2008;28(9):695–706. <http://dx.doi.org/10.1016/j.soildyn.2007.10.018>.
- [19] Gillis K, Dashti S, Hashash Y. Dynamic calibration of tactile sensors for measurement of soil pressure in centrifuge. *ASTM Geotech Test J* 2015;38:261–74.
- [20] Zhang W, Esmailzadeh Seylabi E, Taciroglu E. Validation of a three-dimensional constitutive model for nonlinear site response and soil-structure interaction analyses using centrifuge test data. *Int J Numer Anal Methods Geomech* 2017;41(18):1828–47.